Article

Converting Candlenut Shell Waste into Graphene for Electrode Applications

Rikson Siburian [1,2,3,*], Kerista Tarigan [2,4], Yosia Gopas Oetama Manik [1,2], Fajar Hutagalung [4], Yatimah Alias [5,6], Yong Ching Chan [7], Boon Peng Chang [7], Jonathan Siow [7], Amanda Jiamin Ong [7], Jingfeng Huang [7], Suriati Paiman [8], Boon Tong Goh [9], Lisnawaty Simatupang [10], Ronn Goei [7], Alfred Iing Yoong Tok [7], Mohd Fakharul Zaman Raja Yahya [11] and Fathan Bahfie [12]

1   Department of Chemistry, Faculty of Mathematics and Natural Sciences, Universitas Sumatera Utara, Medan 20155, Indonesia
2   Carbon and Frankincense Research Center, Universitas Sumatera Utara, Medan 20155, Indonesia
3   Department of Physics, Faculty of Mathematics and Natural Sciences, Universitas Sumatera Utara, Medan 20155, Indonesia
4   Department of Chemistry, Faculty of Mathematics and Natural Sciences, Sam Ratulangi University, Jl. Kampus Unsrat Kleak, Manado 95115, Indonesia
5   Faculty of Science, Universiti Malaya, Kuala Lumpur 50603, Malaysia
6   University Malaya Centre for Ionic Liquids (UMCiL), Universiti Malaya, Kuala Lumpur 50603, Malaysia
7   School of Materials Science and Engineering, Nanyang Technological University, 50 Nanyang Avenue, Singapore 639798, Singapore
8   Physics Department, Faculty of Science, Universiti Putra Malaysia, Seri Kembangan 43400, Malaysia
9   Low Dimensional Materials Research Centre, Department of Physics, Faculty of Science, University of Malaya, Kuala Lumpur 50603, Malaysia
10 Department of Chemistry, Faculty of Mathematics and Natural Sciences, Universitas Negeri Medan, Medan 20221, Indonesia
11 Faculty of Applied Sciences, Universiti Teknologi MARA Shah Alam, Shah Alam 40450, Malaysia
12 Research Center for Mining Technology, National Research and Innovation Agency, Jakarta Pusat 10340, Indonesia
*   Correspondence: rikson@usu.ac.id

Abstract: Graphene was synthesized through a two-step pyrolysis method using waste candlenut (*Aleurites moluccanus*) shells as the precursor. Cerium (Ce)/graphene composites were prepared via an impregnation technique. The resulting graphene and Ce/graphene were characterized using various analytical methods, including Scanning Electron Microscopy with Energy-Dispersive Spectroscopy (SEM-EDS), X-ray Diffraction (XRD), X-ray Photoelectron Spectroscopy (XPS), Transmission Electron Microscopy (TEM), Thermo Gravimetric Analysis (TGA), Fourier Transform Infrared (FTIR) spectroscopy, Cyclic Voltammetry (CV), and Linear Sweep Voltammetry (LSV). The bio-carbon produced predominantly exhibited a graphene structure with flat carbon morphology and an interlayer distance of 0.33 nm. This structural information is supported by XRD data, which shows a broad and weak peak at $2\theta = 26°$ corresponding to the C (002) plane, indicative of graphene presence. FTIR, XPS, and Raman spectroscopy further confirmed the presence of graphene through the detection of Csp2 aromatic bonds and the characteristic D, G, and 2D peaks. Notably, the performance of cerium can be enhanced by the incorporation of graphene, attributed to the large surface area and chemical interactions between Ce and graphene. Consequently, candlenut-derived graphene shows potential as a supportive material for modifying the properties of cerium, due to the current value of Ce/Graphene increase with presence of graphene, thereby opening avenues for various advanced applications, such as sustainable and high-performance energy storage systems.

Keywords: graphene; candlenut (*Aleurites moluccanus*) shell; Ce/graphene; carbon large scale production; energy storage electrodes

1. Introduction

The large-scale production of high-quality graphene is a crucial area of research due to its extensive industrial applications [1]. Researchers have reported techniques for producing large-scale graphene, such as chemical vapor deposition (CVD), top-down liquid exfoliation of 2D materials and bottom-up wet chemical synthesis [2]. In this paper, we present a novel technique for producing graphene using renewable materials.

Agriculture production has surged alongside the exponential growth of the world's population over the past 50 years, a trend projected to continue. Consequently, the increase in agricultural waste has become more pronounced [3]. Industries like palm oil, rice, and corn utilize only a fraction of the crops they produce, leaving substantial waste in their wake. For instance, in palm oil production, a mere 10% of the fruit yields oil, while the remainder turns into waste [4]. Unfortunately, improper disposal of this agricultural waste, often through burning, poses serious risks as it releases toxic gases and haze, becoming a potential pollutant and health hazard [5,6].

On the flip side, concerns surrounding excessive consumption of non-renewable fuels have driven extensive research into renewable energy sources. Notably, carbon-based materials have been the focus in energy storage supercapacitors [5]. In order addressing the mounting agricultural waste issue and increasing electrode production costs, researchers turn to carbon-based materials derived from this waste for the supercapacitor electrodes application. Through pyrolysis, the agricultural waste is heated in the absence of oxygen before undergoing chemical or physical activation to yield a porous carbon-based material, graphene, a carbon nanostructure with a large specific surface area [6]. Graphene's abundance of electro-active sites on its surface results in enhanced super capacitive performance, offering superb electronic qualities [7]. Consequently, when employed as electrode material in supercapacitors, these carbon-based materials provide extended cycling life and rapid charging capabilities [5].

While research has been published on doping carbon-based electrodes with elements such as Nitrogen (N), Phosphorus (P), and Boron (B) [8,9]. Doping carbon-based electrodes with these heteroatoms can introduce defects and modify the electronic structure of the carbon material. These heteroatoms can create new active sites for redox reactions during the charging and discharging processes in supercapacitors, leading to improved electrochemical properties and higher specific capacitance [10,11]. Introducing nitrogen into activated carbon has been discovered to enhance capacitance through pseudocapacitive behavior [12,13]. In addition, doping with these elements can increase the surface area of the carbon-based electrode and act as electron donors or acceptors in the carbon lattice, which improves the electrical conductivity of the electrode material [14,15]. Better conductivity translates to faster electron transport during charge and discharge cycles, enhancing the overall performance of the supercapacitor. However, there is ongoing research to explore other doping strategies, such as rare earth metals, to further improve supercapacitor technology and expand its potential applications [16,17]. Only a few studies have explored doping with rare earth metals or other novel materials. This indicates an unexplored realm in the realm of carbon-based electrodes. Therefore, further investigation into carbon-based electrodes doped with rare earth metals is essential to unlock potential advancements in supercapacitor technology and foster sustainable energy solutions.

Rare earth metals, including lanthanoids and actinoids, belong to the f-block transition metals often find applications in nuclear energy, clean energy, and catalysis [18]. When doped into transition metal oxides and hydroxides, they exhibit the ability to enhance electrochemical activity, structural stability, and ionic conductivity of electrode materials. Their large ionic radii and involvement of partially filled 5f orbitals in bonding facilitate improved electronic and ionic transportation during electrochemical reactions [7], making them promising candidates for graphene doping.

In this study, bio-sourced carbons derived from candlenut shells were doped with varying weight percentages (10, 20, and 30 wt.%) of rare earth metals, i.e., Cerium (Ce), known for enhancing redox performance in many industrial catalytic reactions [18], and

Neodymium (Nd), which has shown to improve the electrochemical properties of lithium-ion batteries when doped into LiNiPO$_4$ [19]. The synthesis and fabrication methods of these doped carbons from agricultural waste were characterized using various techniques.

Subsequently, doped carbon samples were employed to modify the surface of glassy carbon electrodes (GCE). Cyclic voltammetry (CV) and linear sweep voltammetry (LSV) were utilized to investigate the electrochemical properties, shedding light on the performance enhancement achieved through rare earth metal doping. This research explores the potential of utilizing agricultural waste-derived graphene doped with rare earth metals as a promising avenue for advanced electrode materials, contributing to the development of sustainable and high-performance energy storage systems.

2. Materials and Methods

2.1. Preparations of Candlenut Graphene Nano Sheets (GNS)

Candlenut shells were subjected to pyrolysis under an argon atmospheric furnace using tube furnace at 600 °C for 5 h to produce charcoal chips. An equal amount of activated carbon was added to the charcoal chips to remove any functional groups formed from oxidation and the mixture was pulverized. This mixture underwent pyrolysis again at 600 °C for 1 h. After cooling, the mixture was washed with water and subsequently dried in an oven at 100–105 °C. The dried mixture was pulverized again and filtered with a 200 mesh to separate powdered GNS from activated carbon. This product was then labelled as Candlenut graphene.

The Mapewrap 31SP epoxy resin was purchased from Mapei Far East Pte. Ltd., Singapore. The resin has a resin-to-hardener mixing ratio of 3:1 by weight, with a working time of 40 min, and a curing duration of 24 h in ambient conditions, as per manufacturer's instructions.

2.2. Doping of GNS

In this experiment, GNS were doped with 10, 20 and 30 wt% Ce, respectively. The 10 wt% Ce/GNS was prepared as follows: 500 mg of GNS powder and 169.5 mg of (CeO$_8$S$_2$)·4H$_2$O crystals were measured out and placed into separate beakers before the addition of 50 mL of ethanol, respectively. The mixtures were then stirred for 1 h using a magnetic stirrer to produce a uniform solution. Subsequently, the GNS solution was mixed with the Ce precursor and stirred for another 3 h. The resulting mixture was dried in an oven at 80 °C for 12 h and then ground into fine powder using a mortar and pestle [20].

2.3. Preparation of Electrodes

After confirming the presence of doped cerium, the fabrication of glassy carbon electrodes (GCEs) coated with doped GNS began. The GCEs were first cleaned by soaking in distilled water and ultrasonicated for 30 min, followed by soaking in ethanol and ultrasonicated for another 30 min. The electrodes were then dried with nitrogen gas and subjected to 30 s cold-plasma cleaning (PiezoBrush PZ3, Relyon Plasma GmbH, Regensburg, Germany) to remove organics residue at the surface of the GCEs. Next, 10 mg of doped GNS powder was added to 0.75 mL of ethanol and ultrasonicated for 30 min. Then, 1 mL of Nafion^{TM} 117 (70160, Sigma-Aldrich, Burlington, MA, USA, ~5% in a mixture of lower aliphatic alcohols and water) was added to the mixture and ultrasonicated for another 30 min to obtain the solution for drop casting. For each sample, 1 cm^2 GCEs were coated evenly with 50 µL of the solution using a dropper and dried thoroughly in an oven at 80 °C for 30 min. This step was repeated 3 times such that each sample has three coatings with a total of 150 µL of solution.

Finally, all biocarbon of Candlenut graphene, Ce/Graphene and electrodes were characterized by using SEM-EDX (JSM-7600F, JEOL, Tokyo, Japan), TEM (ACTEM JEOL JEM-ARM300F, JEOL, Tokyo, Japan), XRD (LabX XRD-600, Shimadzu, Kyoto, Japan), FTIR (Nicolet iS50 FTIR Spectrometer, Thermo, Waltham, MA, USA), XPS (XPS Kratos AXIS Supra, Shimadzu, Kyoto, Japan), TGA (NETZSCH 409C TGA/PerkinElmer DSC 4000, NETZSCH, Selb, Germany, PerkinElmer, Waltham, MA, USA), and Raman spectroscopy

(WITEC Confocal Raman Oxford instruments, 488 nm, 20× o-lens, −2000–3000 cm^{-1}, WITec GmbH, Ulm, Germany).

2.4. Electrochemistry Experiment

Lastly, electrochemical studies of GNS doped with cerium and neodymium were performed with Cyclic Voltammetry (CV) and Linear Sweep Voltammetry (LSV) in a three-electrode system. Redox potential and stability of working electrode (doped GNS on GCE) was observed using CV with platinum (Pt) wire as the counter electrode and Ag/AgCl as the reference electrode. LSV was used to measure the change in overpotential. The 1 M KOH electrolyte solution was prepared by mixing 56.11 g of KOH pallets and 1 L of distilled water in a glass beaker and mixing for 30 min with a magnetic stirrer

2.5. AC Electrical Resistance Experiment

The fabrication process of the epoxy-graphene samples at 0.24 and 2.4 wt% is as follows: the prescribed amount of graphene and acetone was placed in a glass beaker with a mass ratio of 1:20 to create a graphene suspension. Initial mixing was conducted using an IKA overhead stirrer at 600 rpm to disperse larger clumps of graphene powder. This was followed by ultrasonication in a bath sonicator for 1 h to minimize the effect of aggregation. Subsequently, the epoxy resin was added to the graphene-acetone suspension and mixed under the same conditions mentioned earlier to create a uniform resin-graphene-acetone suspension. This suspension was then placed in an oven set at 80 °C overnight to ensure complete evaporation of the acetone. The prescribed amount of hardener by weight was poured into the same mixing cup and stirred using an IKA overhead mechanical stirrer at 1500 rpm for 3 min to ensure homogeneous mixing. Once a consistent graphene-epoxy mixture was obtained, the mixing cup was placed in a vacuum chamber and set to low vacuum for a degassing period of 20 min to remove any entrapped air bubbles introduced during the mixing process. These bubbles could create defects in the cured composite, hindering electrical conductivity. The degassed graphene-epoxy mixture was then poured into silicone rubber molds and allowed to cure in ambient conditions for 24 h. After curing, the epoxy-graphene samples underwent surface preparation methods to remove defects such as bubbles on the surface. The dimensions of each sample were measured using a pair of digital vernier calipers accurate to 0.01 mm. The average dimensions for each sample were 12.63 cm × 1.25 cm × 0.33 cm (Length × Width × Depth).

To measure the AC electrical resistivity of the samples, a handheld LCR meter (model RS-PRO LCR-1703) purchased from RS Components Pte. Ltd., Singapore, was used. The edges of the samples were connected to the LCR meter, and an AC current with a frequency of 1 kHz was applied. After obtaining a stable reading, nine AC resistance measurements were recorded per sample, and the average and standard deviation of these measurements were reported.

3. Results and Discussion

3.1. XRD

XRD analysis was carried out to compare the phases of the graphene crystals synthesized from candlenut to all-variation of percentage Ce doped graphene shown in Figure 1. The presence of nanoscale graphene layers on the interlayer is indicated by the broad and weak peaks detected in the graphene. To calculate the interlayer spacing of graphene, the diffraction peaks must adhere to the Bragg equation, as specified in Equation (1).

$$2d\sin\theta = n\lambda \tag{1}$$

The lattice spacing, designated as d, the angle θ created between the inverse ray and the reflecting crystal plane, the wavelength represented by λ, and the reflection series labelled as n all have significant importance. The reduced interlayer distance of the graphene sheets can be ascribed to the heightened disarray and impairment inside the crystal lattice during

the process of manufacturing graphene. The XRD diffraction pattern of graphene doped with varying weight percentages of Ce are shown in Figure 1.
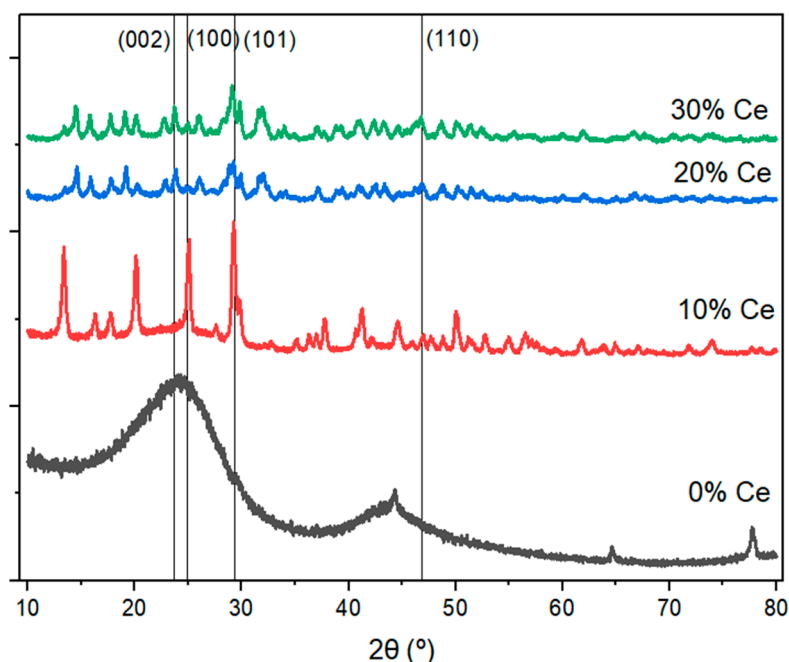

Figure 1. XRD pattern of Graphene (0 wt% Ce) and 10–30 wt% Ce/Graphene.

As seen in Figure 1, the XRD diffractogram graphene results showed peaks at $2\theta = 24.7°$, due to weak graphene layers which correspond to planes (002) which is close to that of graphite at $2\theta = 26°$ due to the interlayer spacing of 0.334 nm confirms the formation of GNSc. After Ce doped graphene, there is a change in the crystalline phase which is marked by the appearance of another diffractogram on the graph. Although the peaks were found to be shifted left by 1°. JCPDS 00-023-1048 Ce_2O_3.

There are three prominent peaks were identified at $2\theta = 25.19, 29.33$, and $31.94°$ (Figure 1), which corresponds to planes (002), (111) and (200) respectively. This suggests the presence of Ce deposited in graphene. The peak at (111) is relatively more intense as compared to the other peaks and is from the cubic face (FCC) (111) lattice plane of CeO_2 [21,22]. Interestingly emergence of new peaks on Ce/graphene indicates the interaction between cerium (Ce) and graphene indeed holds the potential to result in the formation of new crystalline phases.

This interaction implies an intricate many-body phenomenon that has the potential to result in unique crystal structures. Hwang's research indicates that the phenomenon can be explained by the Kondo effect observed when Ce is intercalated, resulting in localized states near the Fermi energy that hybridize with the graphene π-band [21,22]. This hybridization leads to structural changes and the emergence of new peaks.

However, when graphene is doped with Ce, the interaction between Ce and graphene influences several factors, including the appearance of unindexed peaks due to new phases, structural modifications, defects, and impurities. Meanwhile percentage ratio 10%w Ce has a slightly different diffractogram from 20% Ce and 30% C, there is still the influence of graphene due to less Ce concentration so that the weak graphene peak still appears at 10% Ce/Graphene, in this stage 10% Ce doping, there might be a phase transition or the formation of a new crystalline phase at the transition. This could lead to unique diffraction peaks.

3.2. SEM–EDX

Moreover, the SEM EDX data may assist us to make clearer the undoped and doped effect.

The Candlenut graphene has thin and flat surfaces (Figure 2a) and C element is major element containing of graphene (Figure 2b–e). The element containing graphene may be seen in Table 1 (EDX data).
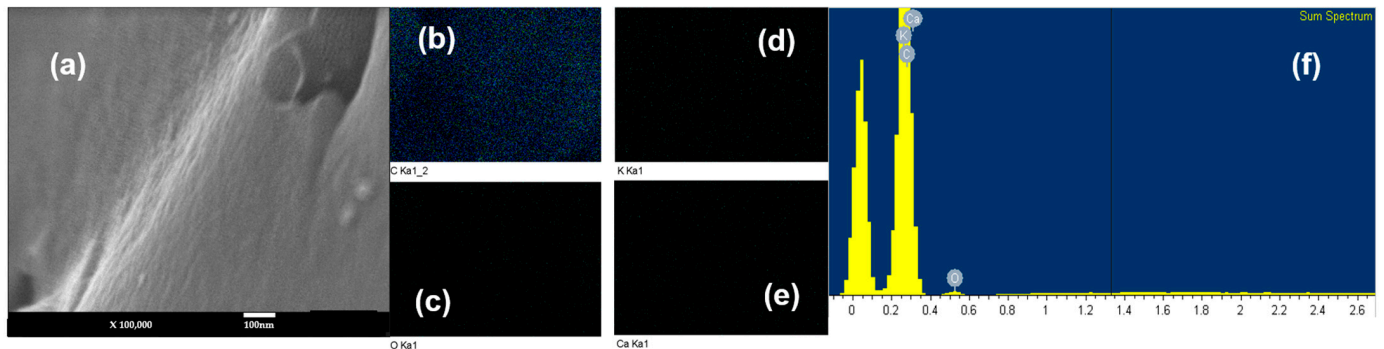

Figure 2. SEM image (**a**); C element mapping (**b**); O element mapping (**c**); K element mapping (**d**); Ca element mapping (**e**); and EDX graph (**f**) for Candlenut graphene.

Table 1. Composition elements of Candlenut graphene.

Element	Weight (%)	Atomic (%)
C	94.95	95.00
O	4.15	4.72
K	0.65	0.20
Ca	0.24	0.07

The SEM EDX data proves that graphene is well formed from candlenut as a raw material with remnant product around 19–21%. The morphological structure of graphene is totally different compared to graphite, graphite oxide, graphene oxide and reduced graphene oxide [23–25]. Interestingly, the C element containing graphene is more than 90 wt.% and it has flat and thin surfaces respect to large surface area. In addition, TEM was also used to characterize graphene to prove that graphene may be produced from candlenut as a raw material (Figure 3).
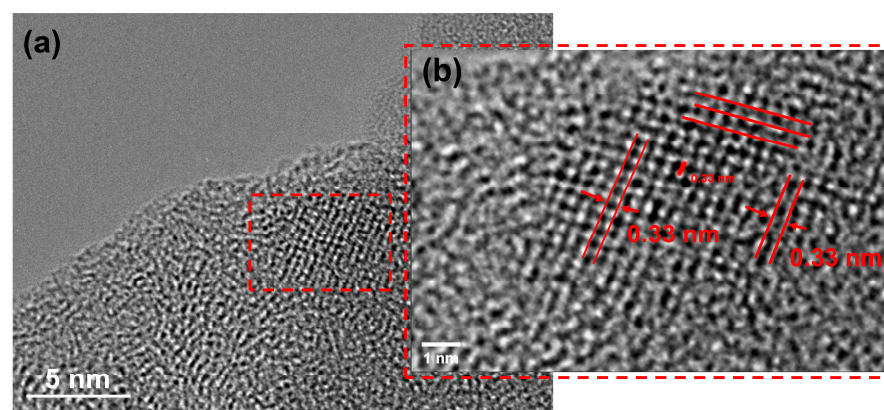
Figure 3. TEM image of Candlenut graphene (**a**) The scale bar is 5 nm and (**b**) 1 nm for the inset.

TEM image (Figure 3) shows the Candlenut graphene has flat, thin, large surface area and d-spacing lattice is 0.33 nm, meaning produced Candlenut graphene is similar to a 2D planar structure of sp^2 hybridized carbon atoms arranged in a honeycomb crystal lattice with an inter-layer spacing [26].

Subsequently, the property of Candlenut graphene was evaluated with Ce deposited on it. SEM EDX was used to analyze them (Figure 4).
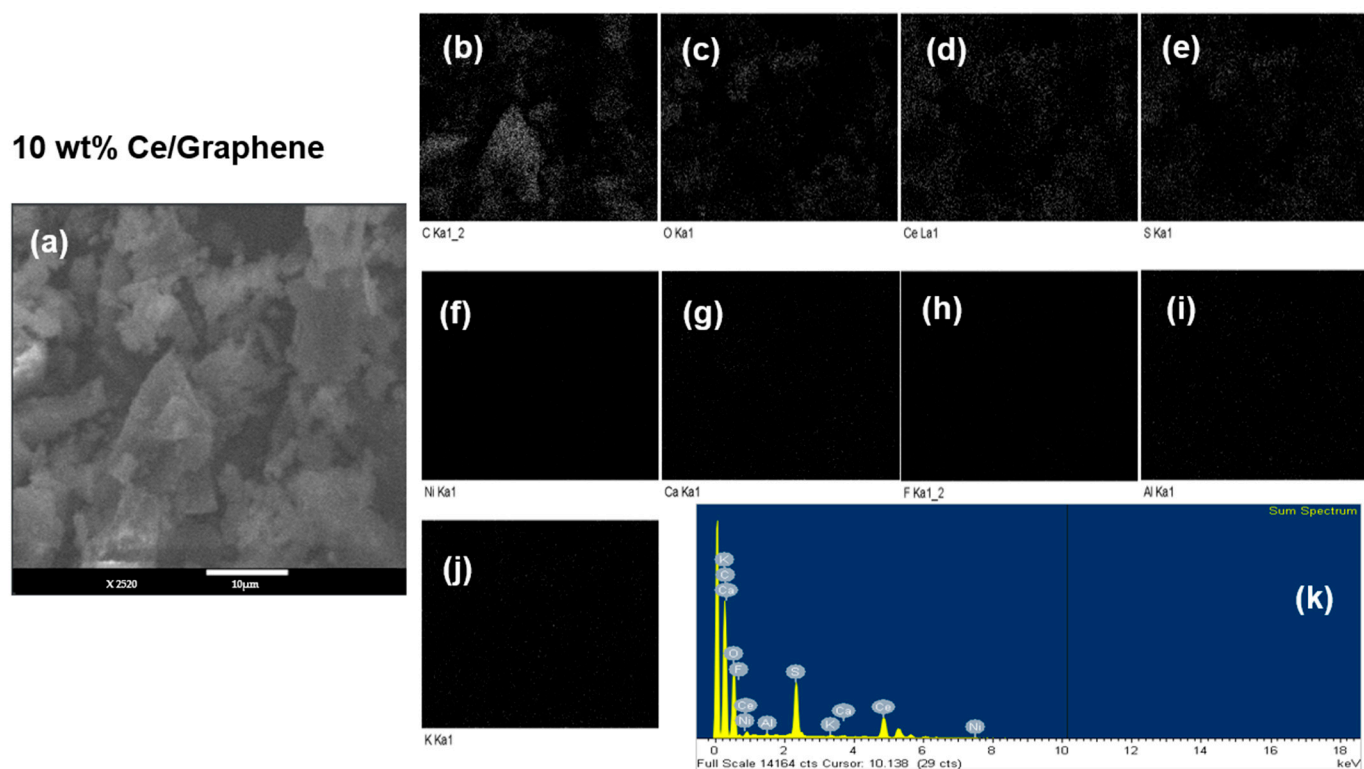
Figure 4. SEM image (**a**); C element mapping (**b**); O element mapping (**c**); Ce element mapping (**d**); S element mapping (**e**); Ni element mapping (**f**); Ca element mapping (**g**); F element mapping (**h**); Al element mapping (**i**); K element mapping (**j**) and EDX graph (**k**) for 10 wt% Ce/Graphene.

Figure 4a,c,k clearly show that C and Ce elements exist on 10 wt.% Ce/Graphene, meaning the Ce is well deposited on graphene. The elements composition of 10 wt% Ce/Graphene may be seen in Table 2.

Table 2. Composition elements of 10 wt% Ce/Graphene.

Element	Weight (%)	Atomic (%)
C	78.49	80.36
O	9.60	9.10
Ce	10.49	10.04
S	0.48	0.19
Ni	0.02	0.03
Ca	0.52	0.16
F	0.10	0.12
Al	0.13	0.06
K	0.30	0.10

More depositing performance of graphene as well as a supporting material, evaluating by depositing variation of Ce on graphene (20 and 30 wt.% Ce/Graphene) are shown (Figure 5I,II).

Figure 5I,II show that Ce particles exist on graphene for both 20 and 30 wt.% Ce/Graphene. The sub-figures show the individual element mapping distribution. These data are very important because (i) graphene base on candlenut shell may be developed as a supporting material; (ii) large scale and sustainable graphene production is possible produced by using simple method and renewable material as a starting material and (iii) there is chemically interaction between Ce and graphene. The elements composition of 20 and 30 wt.% Ce/Graphene can be seen in Table 3.
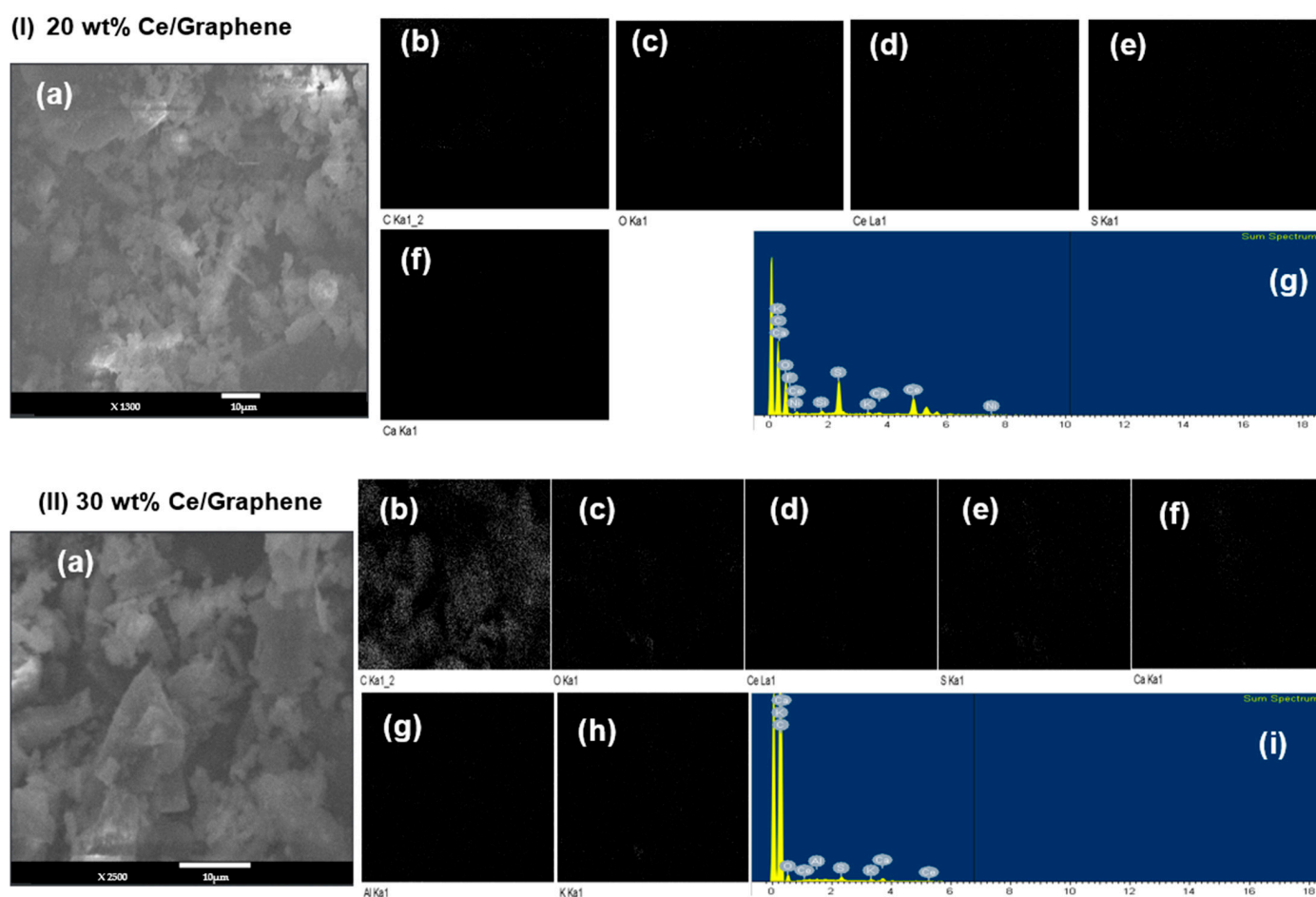
Figure 5. (**I**). SEM image (**a**); C element mapping (**b**); O element mapping (**c**); Ce element mapping (**d**); S element mapping (**e**); Ca element mapping (**f**); EDX graph (**g**) for 20 wt% Ce/Graphene; and (**II**). SEM image (**a**); C element mapping (**b**); O element mapping (**c**); Ce element mapping (**d**); S element mapping (**e**); Ca element mapping (**f**); Al element mapping (**g**); K element mapping (**h**); EDX graph (**i**) for 30 wt% Ce/Graphene.

Table 3. Composition elements of 20 and 30 wt% Ce/Graphene.

	20 wt% Ce/Graphene		30 wt% Ce/Graphene	
Element	**Weight (%)**	**Atomic (%)**	**Weight (%)**	**Atomic (%)**
C	77.13	77.12	67.63	68.03
O	1.43	1.29	1.11	1.47
Ce	20.45	20.64	30.18	30.01
S	0.06	0.51	0.55	0.21
Ni	0.00	0.00	0.00	0.00
Ca	0.27	0.11	0.22	0.05
F	0.00	0.00	0.00	0.00
Al	0.00	0.00	0.12	0.17
K	0.29	0.12	0.19	0.07
Si	0.38	0.21	0.00	0.00

Based on SEM–EDX data (Figures 4 and 5 and Tables 2 and 3) clearly show the Ce atoms are well deposited on graphene and the preparation method of Ce/Graphene may be recognized. In addition, the GNS role is very important to control distribution and size of Ce particles meanwhile there are other metals such as Ca, K, and Si. These metals are contained in biomass as trace metals however the percentage is very low under 0.05% which may be due to pyrolysis that makes trace metal trapped in compounds.

3.3. TGA

Further, the thermal properties of graphene and Ce amount on graphene moreover were evaluated with TGA (Figure 6).
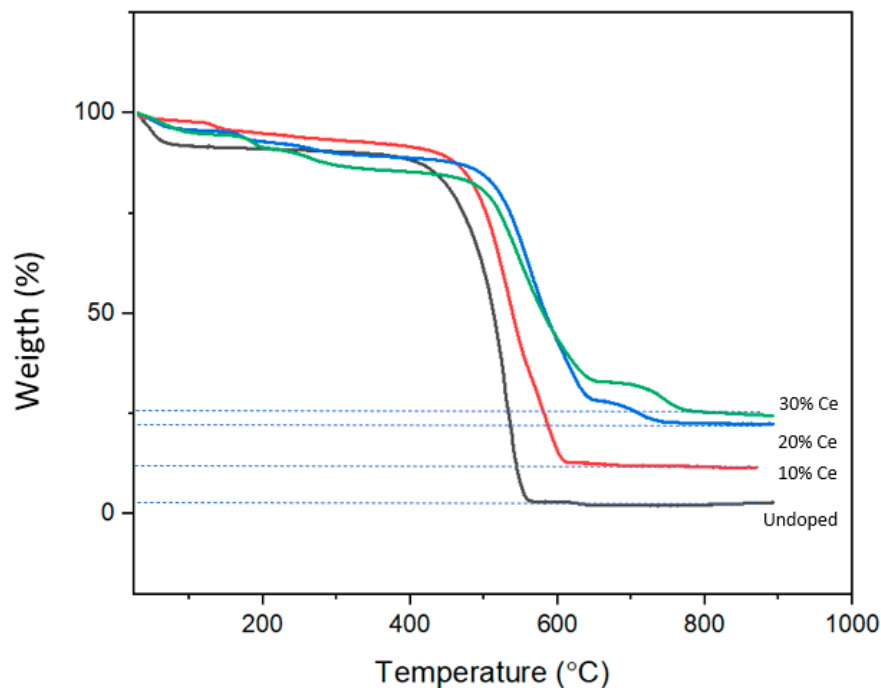

Figure 6. TGA graph of Undoped (graphene), 10, 20 and 30 wt% Ce/Graphene. The dotted line shows the final weight wt% Ce/Graphene at 900°C.

The TGA thermogram in Figure 6 shows the weight percentage with respect to the temperature. The initial gentle decrease of weight percentage seen across all samples could be due to the decomposition of water and other low-molecular-weight compounds [27]. Interestingly, graphene is thermally stable until T = 400 °C and it significantly decreases weight amount with increasing temperature at 400–600 °C and then it is stable again at T = 600–1000 °C, meaning the graphene has the thermally stable performance. The preparation of deposited Ce particles on graphene were well prepared. Each of Ce particles are well deposited on graphene thus the prepared and measured Ce amount are similar, meaning graphene may be expected to control Ce particle sizes.

3.4. FTIR

The FTIR data of graphene and 10–30 wt% Ce/Graphene is presented in Figure 7.

In Figure 7, there is a dip around 1450 to 1700 cm^{-1} which could indicate the presence of aromatic C=C bond and alkene C=C bond which have a range of 1475 to 1625 cm^{-1} and 1635 to 1690 cm^{-1} respectively. There is also a dip near 3450 cm^{-1} that could indicate the presence of hydroxyl group due to the hydrogen bonding interactions between the hydroxyl group and the carbon-hydrogen bond. Figure 7 shows there are two dips in percentage of transmittance, the first dip from 500 to 700 cm^{-1} could be due to lattice vibrations associated with Ce-O-Ce bond angle and Ce-O bond length and the second dip from 900 to 1200 cm^{-1} could be due to asymmetric stretching mode of Ce-O bond. The various functional groups formed through doping could enhance the performance of carbon-based supercapacitor. Oxygen-containing functional groups such as hydroxyl group (-OH) which is present in the doped samples could increase the pseudocapacitance of the carbon-based materials as they act as active sites for adsorption and reaction of electrolyte ions, forming surface-bound charge.
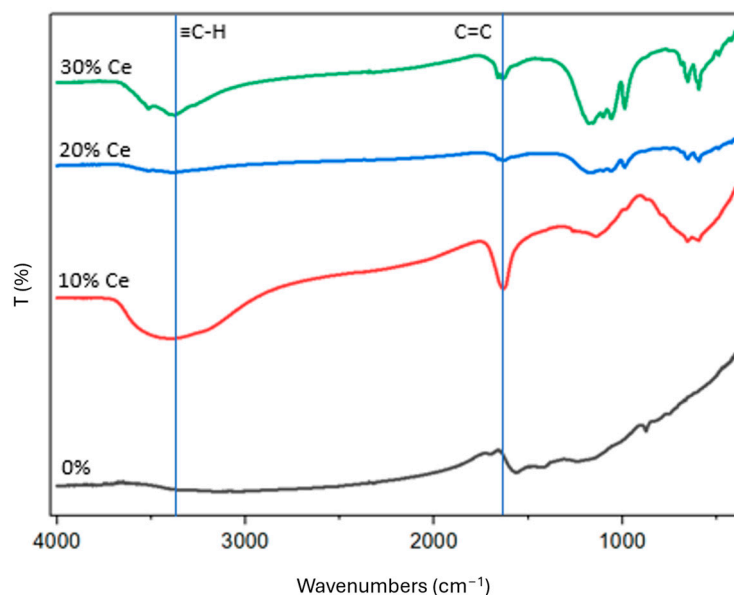
Figure 7. FTIR graph of Candlenut graphene doped with 0, 10, 20 and 30 wt% Ce/Graphene.

3.5. XPS

To further study the bonds present in the graphene and 10–30 wt% Ce/Graphene, XPS measurements were conducted. The XPS spectra of graphene and 10–30 wt% Ce/Graphene may be seen in Figure 8.

Figure 8a shows the XPS graph for C1s, 3 peaks can be observed at 284.8, 286 and 288–290 eV, which corresponds to C-sp^2, C-O and C=O bonds respectively. C=O and sp^2 bonding are typically found in C1s spectrum of Candlenut graphene [28,29]. The presence peak at 284.8 eV is solid evidence to prove the formation of graphene. Note, the XPS spectrum of C1s graphite is 284.5 eV. However, graphene still has oxygen functional group, causing its peak shifts to higher binding energy compared to graphite. That is possible due to the formation of graphene using candlenut shell as a starting material. The pyrolyzed candlenut shell normally produces oxygen functional groups embedded on charcoal. It is then reduced by using non-chemical reductor namely activated carbon, the physically interaction between charcoal and activated carbon may be expected both reducing oxygen functional groups and producing carbon containing graphene like Graphene Nano Sheets (GNS) [30]. Furthermore, the performance of graphene as a supporting material is evaluated with respect to the Ce concentration (10–30 wt% Ce/Graphene) by using XPS. This XPS data is very important to know the chemical interaction between graphene (π-bond) and Ce (f-block metal). Figure 8b shows there are two broad and relatively weak peaks at XPS graph for Ce 3d$_{5/2}$ and Ce 3d$_{3/2}$ located at 879 and 901 eV, which coincides with the Ce (III) oxide binding energy of 875 to 920 eV. The separation of spin-orbit components of Ce 3d$_{3/2}$ and 3d$_{5/2}$ (Δ = 18.6 eV) confirms the presence of Ce dopants within graphene matrix [31,32]. The observation from Cd 3d spectrum is consistent with the O 1s spectrum. There are peaks on binding energy 531.5 and 529 eV (Figure 8c) which correspond to O 1s and metal oxides. Thus, this confirms the presence of Ce oxide with Ce presence in Ce^{3+} oxidation state. The reducing state of Ce (IV) to be Ce (III) may possibly occur be assisted by graphene. Interestingly, the presence of graphene and varies of weight amount of Ce on Ce/Graphene may affect the binding energy position, meaning the catalytic activity of Ce metal can be modified by graphene and weight amount of Ce deposited on Candlenut graphene. The role of Candlenut graphene is very pivotal, mainly acting as a supporting material. The large surface area of graphene may be expected to distribute and deposit much more amount of Ce particles on it. The other role of Candlenut graphene is controlling the particle size and catalytic activity of Ce via chemical interaction between

graphene and Ce [33,34]. These findings are very important to provide and develop the high catalytic activity of Ce catalyst for industry and other applications [35,36].
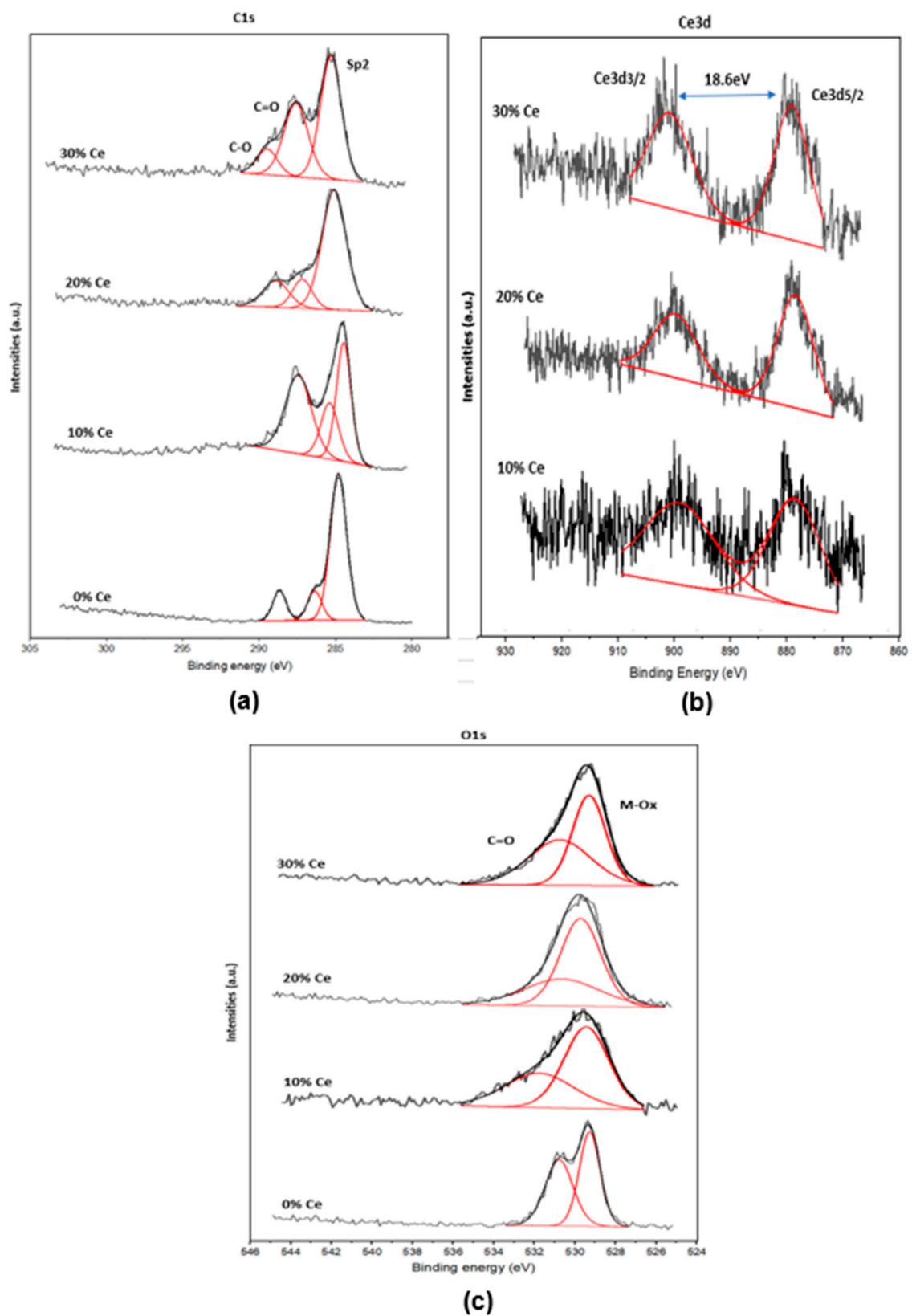

Figure 8. (**a**) C1s, (**b**) Ce 3d and (**c**) O1s XPS graph of Candlenut graphene doped with 0, 10, 20 and 30 wt% Ce.

3.6. Raman

Raman spectroscopy was done on commercial and candlenut graphene to analyze the presence of defects and graphitization of carbon-based materials. As seen in Figure 9.
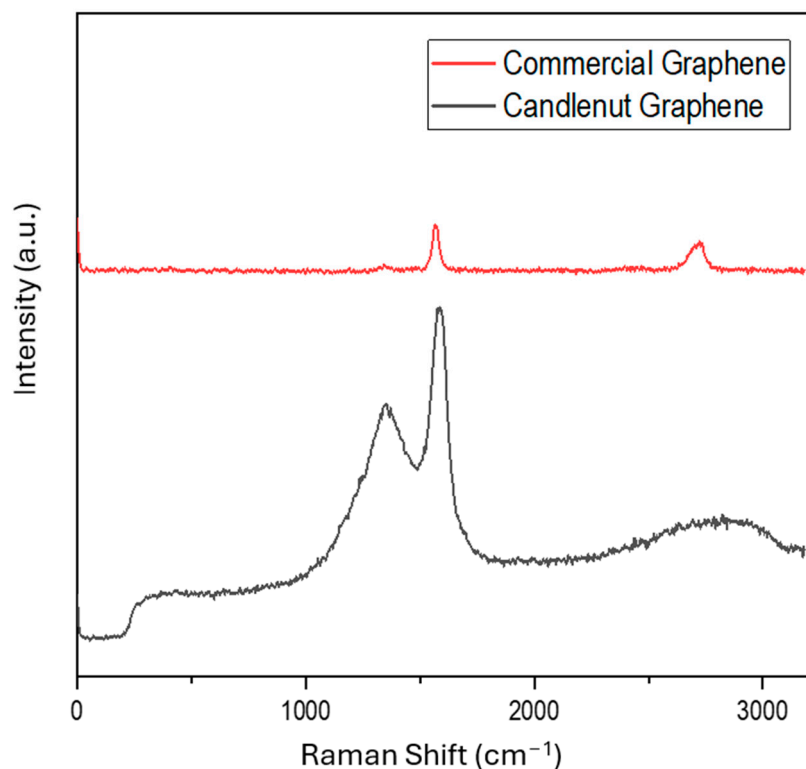

Figure 9. Raman spectra of commercial and Candlenut graphene.

The peak at 1330 cm^{-1} of both materials were matched to the D band which indicates the presence of defects in the crystal lattice which causes the broken symmetry of the hexagonal carbon structure [37,38]. The peak at around 1600 cm^{-1} is matched to the G band which indicates sp^2 hybrid configurations of carbon atoms [39]. Peak around 2697 cm^{-1} is attributed to the 2D band which is used to distinguish the number of layers for carbon structure. A sharp peak was observed for Commercial Graphene which is expected as it represents a monolayer structure which is typical of graphene. The 2D peak for the Candlenut graphene is broad which indicates the presence of multilayered carbon structure [40].

The ratio of the intensity of D band over G band (ID/IG) is used to determine the degree of graphitization of the carbon material. The lower the ID/IG value, the higher the degree of graphitization. As can be seen in Figure 9, the ID/IG (0.98) of the Candlenut graphene is as low as commercial Graphene (0.99) which suggests a very high degree of graphitization and the number of defects. In addition, the Candlenut graphene has lower ID/IG than other biochar that was previously reported [37,39]. A material with higher degree of graphitization has been reported to have higher electrical conductivity [41] and greater electrochemical performance by accelerating ion diffusion [42].

3.7. Electrochemistry Tests

The catalytic activities of Candlenut graphene and 10–30 wt% Ce/Graphene are necessary to observe. The electrochemistry tests those are CV and LSV may be carried out to answer their catalytic activities.

The CV graphs obtained for Candlenut graphene and Ce/Graphene are shown in Figure 10. It should be noted the commercial graphene and Pt are used as well as references on both CV and LSV measurements.
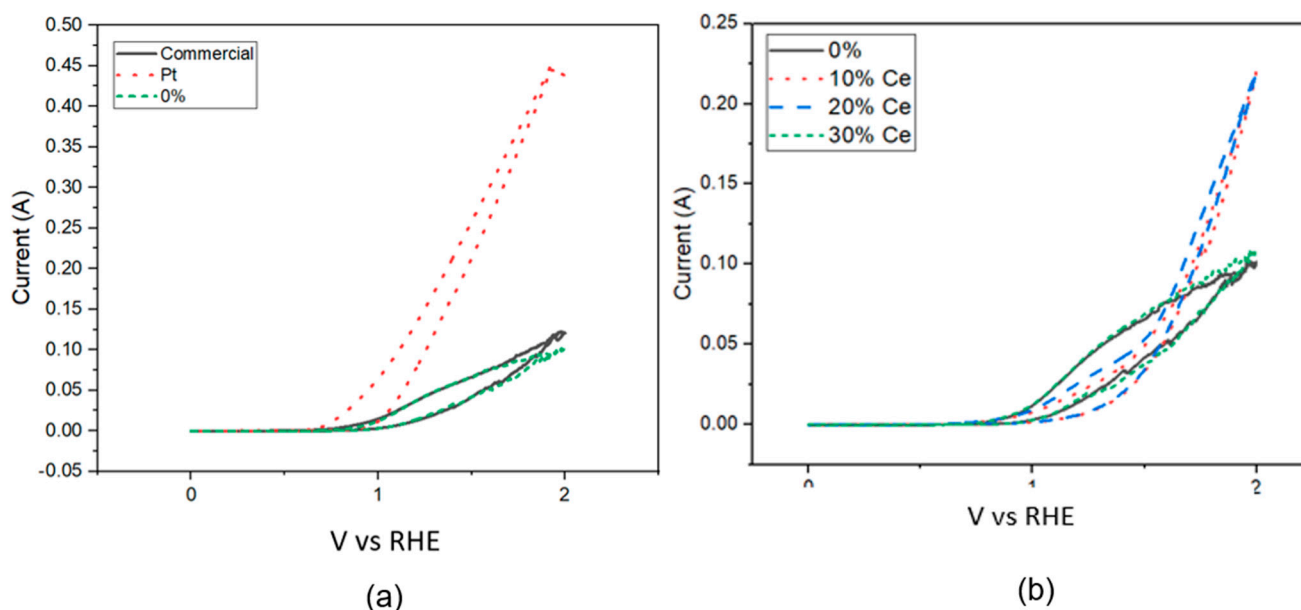
Figure 10. CV graph for (**a**) commercial graphene, platinum, blank GCE and undoped graphene, (**b**) graphene from candlenut doped with 0, 10, 20 and 30 wt% Ce/Graphene.

Figure 10a obviously shows that the current value of commercial graphene is close to Candlenut graphene, however the Pt current value is the highest among others. Interestingly, the current values of 10 and 20 wt% Ce/Graphene are totally different compared to 30 wt% Ce/Graphene (Figure 10b). That is possibly caused the Candlenut graphene as a supporting material and the particle sizes Ce effect. These findings are very important due to the small amount of Ce on Candlenut graphene (10 wt% Ce/Graphene) has higher current compared to 30 wt% Ce/Graphene, meaning the small amount Ce attached on Candlenut graphene may be expected to improve the catalytic activity of Ce. Therefore, the usage Ce amount may be reduced, and it tends to economically cost. The other advantage of this finding is the controlling size, or other properties of Ce may be done when it attaches on Candlenut graphene. Note, 0% (Figure 10a,b) represent to Candlenut graphene.

In addition, the maximum current and area enclosed in the CV graphs may be seen in Table 4.

Table 4. Maximum current and area enclosed of CV graph for each sample.

Working Electrode	Maximum Current (A)	Area Enclosed
Pt	0.4474	0.4932
Blank GCE	0.2184	0.1486
GCE coated with Commercial graphene	0.1224	0.1183
GCE coated with Candlenut graphene	0.1016	0.1096
GCE coated with 10 wt% Ce/Graphene	0.1081	0.1117
GCE coated with 20 wt% Ce/Graphene	0.0944	0.0952
GCE coated with 30 wt% Ce/Graphene	0.0795	0.0815

Based on Table 4, the Candlenut graphene has lower maximum current density of 1016 A cm^{-1} and smaller enclosed area of 0.1096 as compared to commercial graphene which has a maximum current density of 1224 A cm^{-1} and enclosed area of 0.1183, meaning the higher maximum current tends to give higher electrode surface area. However, upon the addition of Ce on Candlenut graphene may decrease its maximum current density and area enclosed numbers. That is caused the Ce state is still Ce oxide. The existence and type of oxygen functional groups on Ce for CeO$_2$ can affect the current density number of CeO$_2$ [43,44]. For Ce doped Candlenut graphene, 10 wt% Ce shows the best results with

a maximum current density of 1081 A cm^{-1} and an enclosed area of 1.117, followed by 20 and 30 wt% Ce/Graphene. This shows that the optimal amounts of dopants to add is 10 wt% for Ce/Graphene. It means the 10 wt% Ce/Graphene has a higher concentration of electroactive species thus faster rate higher electron transfer. However, the Pt working electrode produces the highest maximum current density and area enclosed, however, as mentioned in the literature review, Pt can be quite costly, thus the doped graphene samples made from agricultural waste can be considered as a cheaper alternative. Thus, it can be concluded that graphene doped with 10 wt% Ce yielded the best results when looking at the maximum current and enclosed area of the CV curve. The maximum current, or peak current (I_p) can be used to examine the electrochemical properties. The maximum current density is affected by the concentration of electroactive species in the solution, thus higher maximum current density indicates higher concentration of electroactive species. Higher maximum current density also indicates that a faster rate of electron transfer, and the redox reaction is more favorable. The enclosed area in CV curve, or integrated charge, is proportional to the number of electrons transferred during the redox reaction as well as the electroactive species in the solution [45].

Moreover, analyzing to depict the relationship between overpotential of the anode/cathode and the current density is needed. The LSV analysis and Tafel slope may be expected to address it (Figure 11 and Table 5).
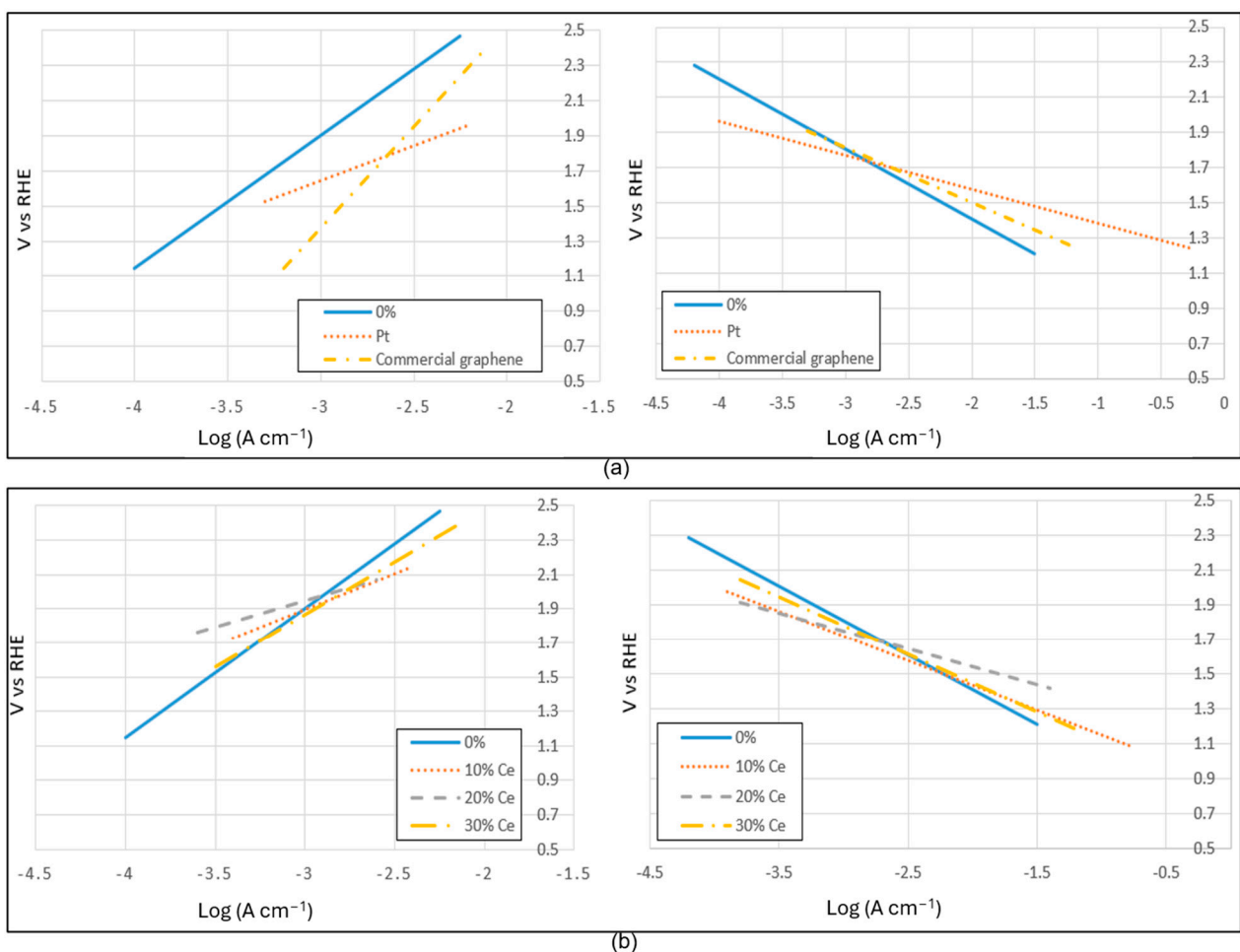

Figure 11. Anodic (**left**) and cathodic (**right**) Tafel slope of (**a**) Commercial graphene, Platinum, blank GCE and Candlenut graphene, (**b**) graphene from candlenut doped with 0, 10, 20 and 30 wt% Ce.

Tafel slope is used to describe the link between overpotential of the anode/cathode and the current density. The anodic Tafel slope describes the rate of oxidation reaction,

where the electrode becomes more positive after losing electrons, thus it illustrates the rate of electron transfer from electrode to the oxidizing species in electrolyte. The cathodic Tafel slope describes the reduction reaction where the electrode becomes more negative after gaining electrons, thus, it illustrates the rate of electron transfer from reducing species in the electrolyte to the electrode. Therefore, catalysts which have smaller Tafel slope value tend to hasten electrocatalytic reaction and lower overpotential [46–49].

The Tafel plot may be seen in Table 5.

Table 5. Anodic, cathodic slope and I_{corr} and E_{corr} obtained from Tafel plot for each sample.

Working Electrode	Anodic Slope	Cathodic Slope	I_{corr} ($\mu A\ cm^{-2}$)	E_{corr} (V)
Pt	0.3966	−0.1951	−2.7829	1.7572
Commercial graphene	1.1489	−0.3131	−2.6894	1.7114
Candlenut graphene	0.7564	−0.3993	−3.0316	1.7308
10 wt% Ce/Graphene	0.3091	−0.2071	−3.3787	1.8387
20 wt% Ce/Graphene	0.4167	−0.2854	−3.1983	1.7708
30 wt% Ce/Graphene	0.6111	−0.3330	−3.0752	1.7641

From Figure 11 and Table 5, the 10 wt% Ce/Graphene has the best results among 20, 30 wt% Ce/Graphene and Candlenut graphene base on Tafel slope data. That is caused it has lower overpotential and faster electrocatalytic reaction. Briefly, the anodic and cathodic slope numbers of 10, 20, 30 wt% and Candlenut graphene are 0.3091, 0.4167, 0.6111, 0.7564 and −0.2071, −0.2854, −0.3330, −0.3993, respectively. Thus, we can see that 10 wt% Ce/Graphene has the best results. These performances are consistent with the CV results where the 10 wt% Ce/Graphene demonstrates the best electrocatalytic activity compared to 20, 30 wt% Ce/Graphene and Candlenut graphene. Thereby, interaction between Ce and Candlenut graphene may affect and modify their electrocatalytic activity properties. The other important property is corrosion resistance property. The best corrosion resistance results (I_{corr} and E_{corr}) are found at 10 wt% Ce/Graphene (−3.3787 $\mu A\ cm^{-2}$ and 1.8387 V), followed 20, 30 wt% Ce/Graphene and Candlenut graphene (Table 5). Interestingly, comparing Ce/Graphene and Pt samples based on corrosion resistance, Ce gives better results compared to Pt. A similar result occurs for Candlenut graphene compares Commercial graphene. Therefore, we can conclude that 10 wt% Ce/Graphene has the best corrosion resistance among others thus it indicates more stable electrode potential [50–54].

Concerning the electrochemistry tests, Candlenut graphene and 10 wt% Ce catalyst achieve better electrochemical measurement results compared to the other weight percentage doped. The 10 wt% Ce/Graphene produces a higher maximum current density and E_{corr} which indicates that it has faster electron transfer and more stable electrode potential. In addition, 10 wt% Ce/Graphene has larger area enclosed within the CV graphs, which indicates higher concentration of electroactive species, gentler anodic and cathodic slope, which indicates lower overpotential and higher electrocatalytic reaction, and higher corrosion resistance, resulting in stronger interactions between Ce and carbon atoms in Candlenut graphene.

3.8. AC Electrical Resistance

To investigate the conductivity of Candlenut graphene and 10–30 wt% Ce/Graphene, we carried out the electrical resistance measurements. The AC electrical resistance measurements are recorded in Table 6.

At a loading level of 0.24 wt.% (Table 6), the composites containing Candlenut graphene and Candlenut graphene powder additives exhibit reduced values of AC electrical resistance compared to the Commercial graphene obtained from Sigma Aldrich. This reduction could be attributed to the presence of functional groups on the surface of the graphene structure, which facilitate better compatibility between the conductive additive and the epoxy resin matrix, improving its dispersion. Furthermore, the lack of significant

improvement in electrical resistance between loading levels at 0.24 and 2.4 wt.% suggests that electrical percolation had already been achieved at the lower loading level.

Table 6. AC electrical resistance measurements for epoxy-graphene samples at frequency of 1 kHz.

Sample	AC Resistance (MΩ)
Commercial Graphene (0.24 wt.%)	5.80 ± 0.40
Candlenut Graphene (0.24 wt.%)	4.10 ± 0.54
Candlenut Graphene-Commercial Graphene (0.24 wt%)	4.42 ± 0.22
Candlenut Graphene-Ce-Commercial Graphene (0.24 wt.%)	4.27 ± 0.29
Candlenut Graphene-Commercial Graphene (2.4 wt%)	4.43 ± 0.22
Candlenut Graphene-N Commercial Graphene (2.4 wt.%)	4.19 ± 0.17
Candlenut Graphene-Fe-Commercial Graphene (2.4 wt.%)	4.35 ± 0.54
Candlenut Graphene-Zn-Commercial Graphene (2.4 wt.%)	4.31 ± 0.26
Candlenut Graphene-Ni-Commercial Graphene (2.4 wt.%)	4.21 ± 0.17

The effect of doping the biocarbon (Candlenut graphene) with various cations to improve electrical conductivity is also studied. Nitrogen (N) and transition metal cations dopants such as iron (Fe), zinc (Zn), and nickel (Ni) showed reductions in AC resistance, with nitrogen-doped graphene demonstrating the most significant improvement in electrical conductivity. However, metal cations belonging to the lanthanide series of the periodic table, such as cerium (Ce) do not show significant improvement. This suggests that the electronic structure of the cationic dopant and its effect on the graphene structure play a crucial role in facilitating the transfer of charge across the composite.

Based on all data, we propose the model of converting Candlenut shell to be carbon containing Graphene (Figure 12).
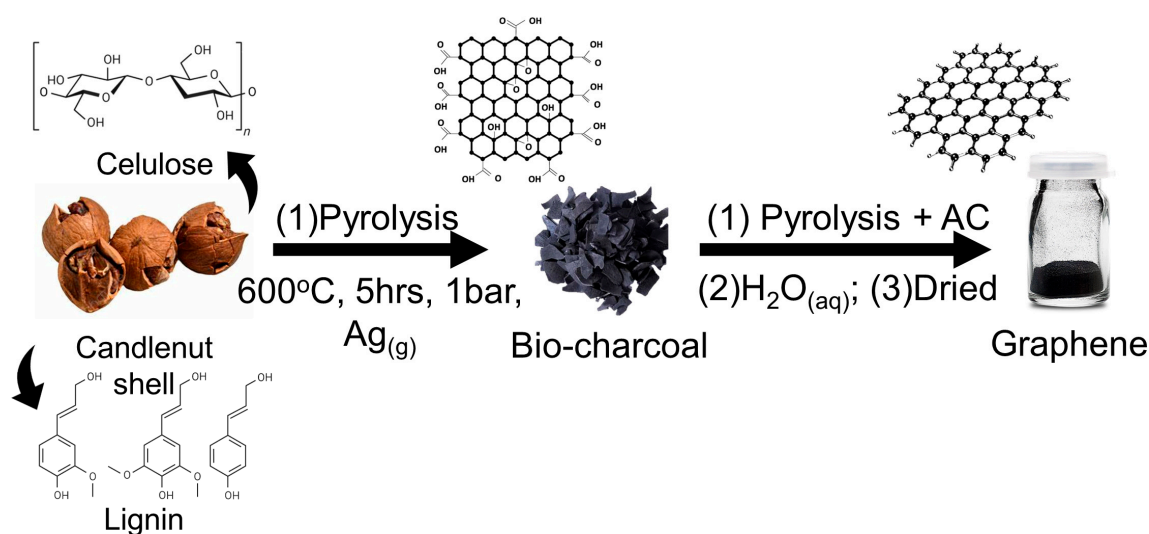

Figure 12. The route of converting Candlenut shells to carbon containing graphene.

Figure 12 shows that there are three steps converting Candlenut shells to be carbon containing graphene namely:

Step-1: Candlenut shells contain lignin and cellulose pyrolyzed to form charcoal chips. In this step, the lignin and cellulose should be oxidized and oxygen functional groups containing on it.

Step-2: To reduce oxygen functional groups and reconstruct graphitic carbon structure, pyrolyzed carbon is reduced and attached with activated carbon and further pyrolyzed to generate carbon containing graphene.

Step-3: Finally, in this step, carbon containing graphene is cleaned with distilled water, dried and grinded to separate between graphene and activated carbon, graphene part is collected and characterized.

This route is a very facile route to produce large scale graphene using sustainable raw material.

4. Conclusions

This study showcases the fabrication of bio-sourced carbons containing graphene (Candlenut graphene) derived from candlenut wastes through a two-step pyrolysis process to yield graphene-like carbon. The great electrode current performance indicates its potential for application toward electrode battery. This research explores the potential of utilizing agricultural waste-derived biocarbon doped with rare earth metals as a promising avenue for advanced electrode materials, contributing to the development of sustainable and high-performance electrode.

Author Contributions: R.S.: Conceptualization, Data curation, Investigation, Methodology, Validation, Funding acquisition, Writing—original draft. K.T.: Validation, Visualization, Writing—original draft. Resources, Investigation. Y.G.O.M.: Investigation, Data curation. F.H.: Visualization. Y.A.: Writing—review & editing. Y.C.C.: Investigation, Data curation. B.P.C.: Writing—review & editing. J.S.: Data curation. A.J.O.: Data curation. J.H.: Writing—review & editing, Visualization. S.P.: Writing—review & editing. B.T.G.: Data curation. L.S.: Project administration, Validation, Investigation, Methodology, Writing—original draft. R.G.: Conceptualization, Investigation, Methodology, Validation, Writing—original draft. A.I.Y.T.: Validation, Conceptualization. M.F.Z.R.Y.: Data curation, Investigation, Methodology, Validation. F.B.: Data curation, Investigation. All authors have read and agreed to the published version of the manuscript.

Data Availability Statement: Data is contained within the article.

Conflicts of Interest: The authors declare no conflicts of interest.

References

1. Choi, S.H.; Yun, S.J.; Won, Y.S.; Oh, C.S.; Kim, S.M.; Kim, K.K.; Lee, Y.H. Large-scale synthesis of graphene and other 2D materials towards industrialization. *Nat. Commun.* **2022**, *13*, 1484. [CrossRef] [PubMed]
2. Lv, P.; Li, X.; Zhang, Z.; Nie, B.; Wu, Y.; Deng, N.; Tian, H.; Ren, T.L.; Wang, G. Industrial-scale production of high-quality graphene sheets by millstone grinders. *J. Phys. D Appl. Phys.* **2022**, *55*, 164022. [CrossRef]
3. Koul, B.; Yakoob, M.; Shah, M.P. Agricultural waste management strategies for environmental sustainability. *Environ. Res.* **2022**, *206*, 112285. [CrossRef] [PubMed]
4. Shahbaz, M.; Taqvi, S.A.A.; Inayat, M.; Inayat, A.; Sulaiman, S.A.; McKay, G.; Al-Ansari, T. Air catalytic biomass (PKS) gasification in a fixed-bed downdraft gasifier using waste bottom ash as catalyst with NARX neural network modelling. *Comput. Chem. Eng.* **2020**, *142*, 107048. [CrossRef]
5. Ali, G.A.M.; Habeeb, O.A.; Algarni, H.; Chong, K.F. CaO impregnated highly porous honeycomb activated carbon from agriculture waste: Symmetrical supercapacitor study. *J. Mater. Sci.* **2019**, *54*, 683–692. [CrossRef]
6. Sukmana, I.F.; Widiatmoko, P.; Nurdin, I.; Devianto; Prakoso, T. Effect of $ZnCl_2$ on properties of graphene produced from palm empty fruit bunch. *IOP Conf. Ser. Mater. Sci. Eng.* **2020**, *778*, 012011. [CrossRef]
7. Arunachalam, S.; Kirubasankar, B.; Pan, D.; Liu, H.; Yan, C.; Guo, Z.; Angaiah, S. Research progress in rare earths and their composites based electrode materials for supercapacitors. *Green Energy Environ.* **2020**, *5*, 259–273. [CrossRef]
8. Chen, L.F.; Lu, Y.; Yu, L.; Lou, X.W.D. Designed formation of hollow particle-based nitrogen-doped carbon nanofibers for high-performance supercapacitors. *Energy Environ. Sci.* **2017**, *10*, 1777–1783. [CrossRef]
9. Zhang, K.; Irmak, S.; Catchmark, J.M. Preparation and properties of heteroatom-doped bacterial cellulose-derived carbonaceous materials. *Carbohydr. Polym. Technol. Appl.* **2023**, *6*, 100400. [CrossRef]
10. Kothandam, G.; Singh, G.; Guan, X.; Lee, J.M.; Ramadass, K.; Joseph, S.; Benzigar, M.; Karakoti, A.; Yi, J.; Kumar, P.; et al. Recent Advances in Carbon-Based Electrodes for Energy Storage and Conversion. *Adv. Sci.* **2023**, *10*, 2301045. [CrossRef]
11. Zhao, Z.; Chen, H.; Zhang, W.; Yi, S.; Chen, H.; Su, Z.; Niu, B.; Zhang, Y.; Long, D. Defect engineering in carbon materials for electrochemical energy storage and catalytic conversion. *Mater. Adv.* **2023**, *4*, 835–867. [CrossRef]
12. Ghosh, S.; Behera, S.K.; Mishra, A.; Casari, C.S.; Ostrikov, K.K. Quantum Capacitance of Two-Dimensional-Material-Based Supercapacitor Electrodes. *Energy Fuels* **2023**, *37*, 17836–17862. [CrossRef]

13. Mao, Y.Q.; Dong, G.H.; Li, Y.Q.; Huang, P.; Fu, S.Y. One-step fabrication of N/O self-doped porous carbon derived from 2-MeIM for high-performance supercapacitor electrode. *J. Energy Storage* **2023**, *74*, 109263. [CrossRef]

14. Fang, Y.; Wang, H.; Ji, S.; Wang, X.; Kannan, P.; Wang, R. N and O co-doped carbon cloth as high-capacitance electrodes for high-energy capacitors. *Diam. Relat. Mater.* **2022**, *129*, 109343. [CrossRef]

15. Li, Z.; Lin, J.; Li, B.; Yu, C.; Wang, H.; Li, Q. Construction of heteroatom-doped and three-dimensional graphene materials for the applications in supercapacitors: A review. *J. Energy Storage* **2021**, *44*, 103437. [CrossRef]

16. Shah, S.S.; Aziz, M.A.; Rasool, P.I.; Mohmand, N.Z.K.; Khan, A.J.; Ullah, H.; Feng, X.; Oyama, M. Electrochemical synergy and future prospects: Advancements and challenges in MXene and MOFs composites for hybrid supercapacitors. *Sustain. Mater. Technol.* **2024**, *39*, e00814. [CrossRef]

17. Benoy, S.M.; Pandey, M.; Bhattacharjya, D.; Saikia, B.K. Recent trends in supercapacitor-battery hybrid energy storage devices based on carbon materials. *J. Energy Storage* **2022**, *52*, 104938. [CrossRef]

18. Pallares, R.M.; Abergel, R.J. Transforming lanthanide and actinide chemistry with nanoparticles. *Nanoscale* **2020**, *12*, 1339. [CrossRef] [PubMed]

19. Karthickprabhu, S.; Vikraman, D.; Kathalingam, A.; Prasanna, K.; Kim, H.S.; Karuppasamy, K. Electrochemical and cycling performance of neodymium (Nd^{3+}) doped $LiNiPO_4$ cathode materials for high voltage lithium-ion batteries. *Mater. Lett.* **2019**, *237*, 224. [CrossRef]

20. Siburian, R.; Paiman, S.; Hutagalung, F.; Ali, A.M.M.; Simatupang, L.; Goei, R.; Rusop, M.M. Facile method to synthesize of magnesium-graphene nano sheets for candidate of primary battery electrode. *Colloid Interface Sci. Commun.* **2022**, *48*, 100612. [CrossRef]

21. Zdorovets, M.V.; Kozlovskiy, A.L. Study of the stability of the structural properties of CeO_2 microparticles to helium irradiation. *Surf. Coat. Technol.* **2020**, *383*, 125286. [CrossRef]

22. Li, J.; He, R.; Guo, G.; Li, Y.; Liao, Y.; Li, Y. Synthesis of Hierarchical Layered Quasi-Triangular $Ce(OH)CO_3$ and Its Thermal Conversion to Ceria with High Polishing Performance. *ACS Omega* **2023**, *8*, 8519–8529. [CrossRef] [PubMed]

23. Chuah, R.; Gopinath, S.C.B.; Anbu, P.; Salimi, M.N.; Yaakub, A.R.W.; Lakshmipriya, T. Synthesis and characterization of reduced graphene oxide using the aqueous extract of *Eclipta prostrata*. *Biotech* **2020**, *10*, 364. [CrossRef] [PubMed]

24. Abaszade, R.G.; Mamedova, S.A.; Agayev, F.H.; Budzulyak, S.I.; Kapush, O.A.; Mamedova, M.A.; Nabiyev, A.M.; Kotsyubynsky, V.O. Synthesis and Characterization of Graphene Oxide Flakes for Transparent Thin Films. *Phys. Chem. Solid State* **2021**, *22*, 595. [CrossRef]

25. Barros, N.G.; Neto, A.C.G.; Vaccioli, K.B.; Angulo, H.R.V.; Silva, L.G.A.; Toffoli, S.M.; Valera, T.S. Graphene Oxide: A Comparison of Reduction Methods. *J. Carbon Res.* **2023**, *9*, 73. [CrossRef]

26. Anagbonu, P.; Ghali, M.; Allam, A. Low-temperature green synthesis of few-layered graphene sheets from pomegranate peels for supercapacitor applications. *Sci. Rep.* **2023**, *13*, 15627. [CrossRef] [PubMed]

27. Chenniappan, T.; Uttamchand, N. Effect of graphene on thermal, mechanical, and shape memory properties of polyurethane nanocomposite. *Appl. Phys. A* **2022**, *128*, 937. [CrossRef]

28. Krishna, D.N.G.; Philip, J. Review on surface-characterization applications of X-ray photoelectron spectroscopy (XPS): Recent developments and challenges. *Appl. Surf. Sci. Adv.* **2022**, *12*, 100332. [CrossRef]

29. Aarva, A.; Sainio, S.; Deringer, V.L.; Caro, M.A.; Laurila, T. X-ray Spectroscopy Fingerprints of Pristine and Functionalized Graphene. *J. Phys. Chem. C* **2021**, *125*, 18234–18246. [CrossRef]

30. Siburian, R.; Ali, A.M.M.; Sebayang, K.; Supeno, M.; Tarigan, K.; Simanjuntak, C.; Aritonang, S.P.; Hutagalung, F. The loading effect of Pt clusters on Pt/graphene nano sheets catalysts. *Sci. Rep.* **2021**, *11*, 2532. [CrossRef]

31. Isaacs, M.A.; Drivas, C.; Lee, R.; Palgrave, R.; Parlett, C.M.A.; Morgan, D.J. XPS surface analysis of ceria-based materials: Experimental methods and considerations. *Appl. Surf. Sci. Adv.* **2023**, *18*, 100469. [CrossRef]

32. Morgan, D.J. Photoelectron spectroscopy of ceria: Reduction, quantification and the myth of the vacancy peak in XPS analysis. *Surf. Interface Anal.* **2023**, *55*, 787–850. [CrossRef]

33. Zou, S.; Zhu, X.; Zhang, L.; Guo, F.; Zhang, M.; Tan, Y.; Gong, A.; Fang, Z.; Ju, H.; Wu, C.; et al. Biomineralization-Inspired Synthesis of Cerium-Doped Carbonaceous Nanoparticles for Highly Hydroxyl Radical Scavenging Activity, Nanoscale Research Letters. *Nanoscale Res. Lett.* **2018**, *13*, 76. [CrossRef] [PubMed]

34. Vári, G.; Óvári, L.; Kiss, J.; Kónya, Z. LEIS and XPS investigation into the growth of cerium and cerium dioxide on Cu(111). *Phys. Chem. Chem. Phys.* **2015**, *17*, 5124–5132. [CrossRef] [PubMed]

35. Della Mea, G.B.; Matte, L.P.; Thill, A.S.; Lobato, F.O.; Benvenutti, E.V.; Arenas, L.T.; Jürgensen, A.; Hergenröder, R.; Poletto, F.; Bernardi, F. Tuning the oxygen vacancy population of cerium oxide (CeO_{2-x}, $0 < x < 0.5$) nanoparticles. *Appl. Surf. Sci.* **2017**, *422*, 1102–1112. [CrossRef]

36. Yaacov, A.B.; Falling, L.J.; David, R.B.; Attia, S.; Andrés, M.A.; Nemšák, S.; Eren, B. Oxidation and Reduction of Polycrystalline Cerium Oxide Thin Films in Hydrogen. *J. Phys. Chem. Lett.* **2023**, *14*, 7354–7360. [CrossRef] [PubMed]

37. Hourcade, M.G.; Reis, G.S.; Grimm, A.; Dinh, V.M.; Lima, E.C.; Larsson, S.H.; Gentili, F.G. Microalgae biomass as a sustainable precursor to produce nitrogen-doped biochar for efficient removal of emerging pollutants from aqueous media. *J. Clean. Prod.* **2022**, *348*, 131280. [CrossRef]

38. Omiri, J.; Snoussi, Y.; Bhakta, A.K.; Truong, S.; Ammar, S.; Khalil, A.M.; Jouini, M.; Chehimi, M.M. Citric-Acid-Assisted Preparation of Biochar Loaded with Copper/Nickel Bimetallic Nanoparticles for Dye Degradation. *Colloids Interfaces* **2022**, *6*, 18. [CrossRef]

39. Ji, R.; Wu, Y.; Bian, Y.; Song, Y.; Sun, Q.; Jiang, X.; Zhang, L.; Han, J.; Cheng, H. Nitrogen-doped porous biochar derived from marine algae for efficient solid-phase microextraction of chlorobenzenes from aqueous solution. *J. Hazard. Mater.* **2021**, *407*, 124785. [CrossRef]

40. Yan, Y.; Manickam, S.; Lester, E.; Wu, T.; Pang, C.H. Synthesis of graphene oxide and graphene quantum dots from miscanthus via ultrasound-assisted mechano-chemical cracking method. *Ultrason. Sonochem.* **2021**, *73*, 105519. [CrossRef]

41. Cheng, D.; Tian, M.; Wang, B.; Zhang, J.; Chen, J.; Feng, X.; He, Z.; Dai, L.; Wang, L. One-step activation of high-graphitization N-doped porous biomass carbon as advanced catalyst for vanadium redox flow battery. *J. Colloid Interface Sci.* **2020**, *572*, 216–226. [CrossRef] [PubMed]

42. Sun, W.; Bai, J.; Li, C.; Liu, J. Effect of graphitization degree of electrospinning carbon fiber on catalytic oxidation of styrene and electrochemical properties. *Chem. Phys. Lett.* **2019**, *715*, 299–309. [CrossRef]

43. Qiu, C.; Zhou, Q.; Gao, R.; Guo, Y.; Qin, J.; Wang, D.; Song, Y. An Unprecedented CeO_2/C Non-Noble Metal Electrocatalyst for Direct Ascorbic Acid Fuel Cells. *Nanomaterials* **2023**, *13*, 2669. [CrossRef] [PubMed]

44. Shaheen, I.; Hussain, I.; Zahra, T.; Javed, M.S.; Shah, S.S.A.; Khan, K.; Hanif, M.B.; Assiri, M.A.; Said, Z.; Arifeen, W.U.; et al. Recent advancements in metal oxides for energy storage materials: Design, classification, and electrodes configuration of supercapacitor. *J. Energy Storage* **2023**, *72*, 108719. [CrossRef]

45. Elgrishi, N.; Rountree, K.J.; McCarthy, B.D.; Rountree, E.S.; Eisenhart, T.T.; Dempsey, J.L. A Practical Beginner's Guide to Cyclic Voltammetry. *J. Chem. Educ.* **2018**, *95*, 197–206. [CrossRef]

46. Wan, C.; Ling, Y.; Wang, S.; Pu, H.; Huang, Y.; Duan, X. Unraveling and Resolving the Inconsistencies in Tafel Analysis for Hydrogen Evolution Reactions. *ACS Cent. Sci.* **2024**, *10*, 658–665. [CrossRef] [PubMed]

47. Sabir, A.S.; Pervaiz, E.; Khosa, R.; Sohail, U. An inclusive review and perspective on Cu-based materials for electrochemical water splitting. *RSC Adv.* **2023**, *13*, 4963–4993. [CrossRef] [PubMed]

48. Anantharaj, S.; Noda, S.; Jothi, V.R.; Yi, S.C.; Driess, M.; Menezes, P.W. Strategies and Perspectives to Catch the Missing Pieces in Energy-Efficient Hydrogen Evolution Reaction in Alkaline Media. *Angew. Chem. Int. Ed. Engl.* **2021**, *60*, 18981–19006. [CrossRef] [PubMed]

49. Gebremariam, G.K.; Jovanović, A.Z.; Pašti, I.A. The Effect of Electrolytes on the Kinetics of the Hydrogen Evolution Reaction. *Hydrogen* **2023**, *4*, 776–806. [CrossRef]

50. Saji, V.S. Corrosion and Materials Degradation in Electrochemical Energy Storage and Conversion Devices. *ChemElectroChem* **2023**, *10*, e202300136. [CrossRef]

51. Fang, X.; Wu, D.; Liu, J.; Yang, Y.; Lv, S.; Wu, S.; Chen, Y. Microstructure evolution and corrosion resistance of high-pressure rheo-cast Mg–Zn–Y alloy containing quasicrystal. *J. Mater. Res. Technol.* **2023**, *24*, 542–556. [CrossRef]

52. Sotillo, A.F.; Aparicio, P.F. Durable corrosion-resistant coating based in graphene oxide for cost-effective fuel cells components. *iScience* **2023**, *26*, 106569. [CrossRef] [PubMed]

53. Wirtanen, T.; Prenzel, T.; Tessonnier, J.P.; Waldvogel, S.R. Cathodic Corrosion of Metal Electrodes—How to Prevent It in Electroorganic Synthesis. *Chem. Rev.* **2021**, *121*, 10241–10270. [CrossRef] [PubMed]

54. Weia, L.; Gao, Z. Recent research advances on corrosion mechanism and protection, and novel coating materials of magnesium alloys: A review. *RSC Adv.* **2023**, *13*, 8427–8463. [CrossRef]